JOURNAL OF SPACECRAFT AND ROCKETS
Vol. 48, No. 3, May–June 2011

Reduced Model for Flexible Solar Sail Dynamics

Qing Li*
Tsinghua University, 100084 Beijing, People's Republic of China
Xingrui Ma†
China Aerospace Science and Technology Corporation, 100037 Beijing, People's Republic of China
and
Tianshu Wang‡
Tsinghua University, 100084 Beijing, People's Republic of China

DOI: 10.2514/1.48789

In this paper, a reduced model for flexible solar sail dynamics was formulated in mixed coordinates. Foreshortening effects due to the foreshortening deformation of sails and booms were considered. For instance, the dynamic responses of a five-point connected square solar sail during maneuvers were investigated using this reduced model. A time-varying modal stiffness matrix was used to simulate time-varying properties of modal frequencies, due to the change of the solar pressure load. The reduced model was highly efficient using the modal reduction techniques. Its accuracy was verified using a high-fidelity finite element model in ABAQUS/Explicit. It was illustrated that the reduced model can be both efficient and accurate for engineering applications.

Nomenclature

c	=	speed of light, m/s
I_s	=	solar intensity, W
$\boldsymbol{K}_f$	=	modal stiffness matrix, N/m
m_{tot}	=	total mass of the solar sail, kg
n	=	modal reduced order
$\boldsymbol{n}_z$	=	unit normal vector to the reference plane
p_O	=	solar pressure at Point O, Pa
$\boldsymbol{p}_s$	=	solar pressure load vector, Pa
$\boldsymbol{q}$	=	modal coordinate vector, m
$q_i(t)$	=	ith-order modal coordinate, m
$\boldsymbol{R}_O$	=	global position vector of Point O, m
$\boldsymbol{r}_f$	=	local position vector in the undeformed state with respect to Point O, m
$\boldsymbol{u}_f$	=	local displacement vector of an arbitrary point on the solar sail, m
$w(x, y, t)$	=	transverse deflection on the neutral surface, m
(x_0, y_0)	=	reference point on the neutral surface with zero longitudinal displacement, m
$\boldsymbol{\Phi}$	=	mode shape matrix
$\phi_i(x, y)$	=	ith-order mode shape function
Ω_i	=	ith-order modal angular frequency, rad/s
$\boldsymbol{\omega}$	=	angular velocity vector of the body frame with respect to the inertial frame, rad/s
$\dot{}$	=	first time derivative with respect to the inertial frame, s^{-1}
$\ddot{}$	=	second time derivative with respect to the inertial frame, s^{-2}
$\sim$	=	cross-product matrix

Superscripts

$'$	=	first time derivative with respect to the body frame, s^{-1}
$''$	=	second time derivative with respect to the body frame, s^{-2}

I. Introduction

FOR many years, solar sailing has attracted great interest as a method for interstellar travel [1]. Nowadays, several space agencies worldwide are trying to put this idea into practice. A solar sail spacecraft gains momentum by reflecting sunlight photons, forming a macroeffect of solar pressure. Sunlight is both cost-effective and inexhaustible; no additional fuel is needed to propel the spacecraft. However, the solar pressure is quite weak and decreases with the square of the distance from the sun. Therefore, a solar sail must be large and lightweight to gain enough acceleration. Square, disk, and heliogyro configurations have been proposed. A square sail is simpler to operate than a heliogyro sail with long blades of film, and it requires shorter support booms than a disk sail to obtain the same sail area [2]. Consequently, a square is generally the optimum choice of configuration.

The structure of a large solar sail is highly flexible and should be stabilized by geometrically nonlinear effects. Taleghani et al. [3] analyzed a 70 m per edge square sail and a 150 m per edge square sail using two finite element programs, MSC/NASTRAN and ABAQUS. Considering geometrically nonlinear effects in the models, they compared deformations and vibration modes of the solar sails obtained by the two programs. Based on this work, parametric studies of two square solar sail designs (the five-point connected sail and the multiple-point connected sail) were conducted using ABAQUS, which showed the effects of sail size, sail membrane prestress, sail membrane thickness, and boom stiffness on the sail membrane, as well as boom deformations, boom loads, and vibration frequencies [4]. For the use of control for the solar sail, a rigid-flexible coupling model is required. Though a finite element model is high-fidelity, it is quite time-intensive for the control design. Therefore, a reduced model with satisfactory accuracy and efficiency is actually needed. Smith et al. [5] proposed two idealized two-dimensional models and a reduced three-dimensional finite element model for solar sail control. However, the reduced model, which was obtained via Guyan reduction, was not quantitatively verified.

Received 4 January 2010; revision received 20 January 2011; accepted for publication 24 January 2011.

*Ph.D. Candidate, School of Aerospace; qing-li05@mails.tsinghua.edu.cn.
†Professor, China Aerospace Science and Technology Corporation; maxr@spacechina.com.
‡Professor, School of Aerospace; tswang@tsinghua.edu.cn.

Moreover, Guyan reduction completely ignores dynamics of slave degrees of freedom by describing them as a linear function of master degrees of freedom, which leads to an overestimation of the natural frequencies [6]. Therefore, a more accurate and convincing reduced model for a three-dimensional solar sail is necessary.

In the current research, a three-dimensional solar sail model was formulated in mixed coordinates, considering foreshortening effects due to foreshortening deformation [7,8]. Prestressed modes, as obtained in [4] via finite element method, were used to reduce the model in the floating frame of reference. Modal characteristics of the solar sail varying with the solar pressure load were also considered in the reduced model. The accuracy of the reduced model was verified using ABAQUS/Explicit.

II. Reduced Model and Formulations

As shown in Fig. 1, O_0XYZ is the global inertial frame of reference, and $Oxyz$ is the floating frame of reference, i.e., the body frame. The origin of the body frame attaches on the hub of the solar sail.

A. Deformation Kinematics

The main flexible structures of a solar sail are booms and sails. The booms are regarded as Euler–Bernoulli beams, and the sails are regarded as thin plates. As they are coupled, they should be modeled as a whole.

The global position vector of an arbitrary point on the solar sail with respect to O_0 is defined as

$$\boldsymbol{R} = \boldsymbol{R}_O + \boldsymbol{r}_f + \boldsymbol{u}_f \tag{1}$$

The first time derivative of $\boldsymbol{R}$ is

$$\dot{\boldsymbol{R}} = \dot{\boldsymbol{R}}_O + \boldsymbol{\omega} \times (\boldsymbol{r}_f + \boldsymbol{u}_f) + \boldsymbol{u}'_f \tag{2}$$

The second time derivative of $\boldsymbol{R}$ is

$$\ddot{\boldsymbol{R}} = \ddot{\boldsymbol{R}}_O + \dot{\boldsymbol{\omega}} \times (\boldsymbol{r}_f + \boldsymbol{u}_f) + \boldsymbol{u}''_f + \boldsymbol{\omega} \times [\boldsymbol{\omega} \times (\boldsymbol{r}_f + \boldsymbol{u}_f)] + 2\boldsymbol{\omega} \times \boldsymbol{u}'_f \tag{3}$$

Considering the transverse deflection $w(x, y, z)$ and the deduced deformations, $\boldsymbol{u}_f$ is written with respect to $Oxyz$ as

$$\boldsymbol{u}_f = \boldsymbol{u}_{fl} + \boldsymbol{u}_{fs} \tag{4}$$

where $\boldsymbol{u}_{fl}$ is the linear deformation, and $\boldsymbol{u}_{fs}$ is the foreshortening deformation. They are, respectively, expressed as

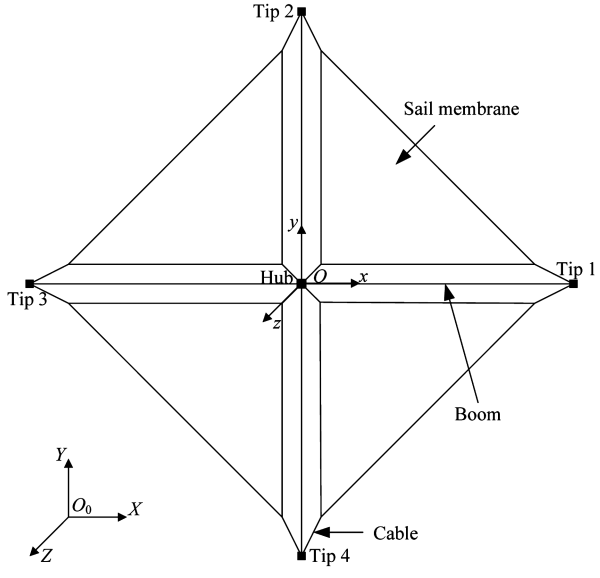

Fig. 1 Representation of a five-point connected square solar sail.

$$\boldsymbol{u}_{fl} = \begin{bmatrix} -z\frac{\partial w(x,y,t)}{\partial x} & -z\frac{\partial w(x,y,t)}{\partial y} & w(x,y,t) \end{bmatrix}^T \tag{5}$$

$$\boldsymbol{u}_{fs} = \begin{bmatrix} -\frac{1}{2}\int_{x_0}^{x}\left(\frac{\partial w(x,y,t)}{\partial x}\right)^2 \mathrm{d}x & -\frac{1}{2}\int_{y_0}^{y}\left(\frac{\partial w(x,y,t)}{\partial y}\right)^2 \mathrm{d}y & 0 \end{bmatrix}^T \tag{6}$$

where (x_0, y_0) is the point with no deformation on the neutral surface, i.e. Point O.

A conventional formulation is derived without considering the foreshortening deformation in Eq. (4). In the following, the foreshortening deformation is included in the derivation, which is called a foreshortening formulation.

The transverse deflection is represented in the modal coordinates as

$$w(x, y, t) = \boldsymbol{\Phi}\boldsymbol{q} = \sum_{i=1}^{n} \phi_i(x, y) q_i(t) \tag{7}$$

where

$$\boldsymbol{\Phi} = [\,\phi_1(x, y) \quad \phi_2(x, y) \quad \cdots \quad \phi_n(x, y)\,] \tag{8}$$

$$\boldsymbol{q} = [\,q_1(t) \quad q_2(t) \quad \cdots \quad q_n(t)\,]^T \tag{9}$$

Prestressed mode shapes of the solar sail are used in Eq. (8).

Substituting Eq. (7) into Eqs. (4) yields

$$\boldsymbol{u}_f = \begin{bmatrix} -z\frac{\partial \boldsymbol{\Phi}}{\partial x} - \frac{1}{2}\boldsymbol{q}^T\boldsymbol{H}_x \\ -z\frac{\partial \boldsymbol{\Phi}}{\partial y} - \frac{1}{2}\boldsymbol{q}^T\boldsymbol{H}_y \\ \boldsymbol{\Phi} \end{bmatrix} \boldsymbol{q} \tag{10}$$

where

$$\boldsymbol{H}_x = \int_{x_0}^{x} \frac{\partial \boldsymbol{\Phi}^T}{\partial x}\frac{\partial \boldsymbol{\Phi}}{\partial x}\,\mathrm{d}x \tag{11}$$

$$\boldsymbol{H}_y = \int_{y_0}^{y} \frac{\partial \boldsymbol{\Phi}^T}{\partial y}\frac{\partial \boldsymbol{\Phi}}{\partial y}\,\mathrm{d}y \tag{12}$$

B. Dynamic Equations

The application of the variational procedure gives the principle of virtual power in the form

$$-\int_V \delta\dot{\boldsymbol{R}} \cdot \ddot{\boldsymbol{R}}\,\mathrm{d}m + \int_A \delta\dot{\boldsymbol{R}} \cdot \boldsymbol{p}_s\,\mathrm{d}A - \delta\dot{\boldsymbol{q}}^T\boldsymbol{K}_f\boldsymbol{q} = 0 \tag{13}$$

Gravities, drag forces, and control forces are not contained in Eq. (13), which can be added in further studies.

Substituting Eqs. (2) and (3) into Eq. (13), one obtains [9]

$$\begin{cases} m_{\mathrm{tot}}\ddot{\boldsymbol{R}}_O - \boldsymbol{S}_f \times \dot{\boldsymbol{\omega}} + \int_V \boldsymbol{u}''_f\,\mathrm{d}m + \boldsymbol{Q}_{ft} = \boldsymbol{F}_t \\ \boldsymbol{S}_f \times \ddot{\boldsymbol{R}}_O + \boldsymbol{J}_f \cdot \dot{\boldsymbol{\omega}} + \int_V (\boldsymbol{r}_f + \boldsymbol{u}_f) \times \boldsymbol{u}''_f\,\mathrm{d}m + \boldsymbol{Q}_{fr} = \boldsymbol{F}_r \\ \boldsymbol{C}_t^T\ddot{\boldsymbol{R}}_O + \boldsymbol{C}_r^T\dot{\boldsymbol{\omega}} + \int_V \boldsymbol{\Phi}_{\mathrm{NL}}^T\boldsymbol{u}''_f\,\mathrm{d}m + \boldsymbol{K}_f\boldsymbol{q} + \boldsymbol{Q}_{ff} = \boldsymbol{F}_f \end{cases} \tag{14}$$

where

$$\boldsymbol{S}_f = \int_V (\boldsymbol{r}_f + \boldsymbol{u}_f)\,\mathrm{d}m \tag{15}$$

$$\boldsymbol{Q}_{ft} = \boldsymbol{\omega} \times (\boldsymbol{\omega} \times \boldsymbol{S}_f) + 2\boldsymbol{\omega} \times \int_V \boldsymbol{u}'_f\,\mathrm{d}m \tag{16}$$

$$\boldsymbol{J}_f = \int_V [(\boldsymbol{r}_f + \boldsymbol{u}_f) \cdot (\boldsymbol{r}_f + \boldsymbol{u}_f)\boldsymbol{I}_3 - (\boldsymbol{r}_f + \boldsymbol{u}_f)(\boldsymbol{r}_f + \boldsymbol{u}_f)]\,\mathrm{d}m \tag{17}$$

$$\boldsymbol{Q}_{fr} = \boldsymbol{\omega} \times (\boldsymbol{J}_f \cdot \boldsymbol{\omega}) + 2\int_V (\boldsymbol{r}_f + \boldsymbol{u}_f) \times (\boldsymbol{\omega} \times \boldsymbol{u}'_f)\,\mathrm{d}m \tag{18}$$

$$\boldsymbol{F}_t = \int_A \boldsymbol{p}_s \,\mathrm{d}A \tag{19}$$

$$\boldsymbol{F}_r = \int_A (\boldsymbol{r}_f + \boldsymbol{u}_f) \times \boldsymbol{p}_s \,\mathrm{d}A \tag{20}$$

$$\boldsymbol{F}_f = \int_A \boldsymbol{\Phi}_{\mathrm{NL}}^T \boldsymbol{p}_s \,\mathrm{d}A \tag{21}$$

$$\boldsymbol{\Phi}_{\mathrm{NL}} = \begin{bmatrix} -z\frac{\partial \boldsymbol{\Phi}}{\partial x} - \boldsymbol{q}^T \boldsymbol{H}_x \\ -z\frac{\partial \boldsymbol{\Phi}}{\partial y} - \boldsymbol{q}^T \boldsymbol{H}_y \\ \boldsymbol{\Phi} \end{bmatrix} \tag{22}$$

$$\boldsymbol{C}_t = \int_V \boldsymbol{\Phi}_{\mathrm{NL}} \,\mathrm{d}m \tag{23}$$

$$\boldsymbol{C}_r = \int_V (\boldsymbol{r}_f \widetilde{+} \boldsymbol{u}_f) \boldsymbol{\Phi}_{\mathrm{NL}} \,\mathrm{d}m \tag{24}$$

$$\boldsymbol{Q}_{ff} = \int_V \boldsymbol{\Phi}_{\mathrm{NL}}^T [\tilde{\boldsymbol{\omega}}\, \tilde{\boldsymbol{\omega}} (\boldsymbol{r}_f + \boldsymbol{u}_f) + 2\tilde{\boldsymbol{\omega}} \boldsymbol{u}_f'] \,\mathrm{d}m \tag{25}$$

Using the four Euler parameters $\boldsymbol{\Lambda} = [\lambda_0 \quad \lambda_1 \quad \lambda_2 \quad \lambda_3]^T$ to describe the attitude position, Eqs. (14) can be written in a matrix form with respect to $Oxyz$ as

$$\boldsymbol{M} \begin{bmatrix} \ddot{\boldsymbol{R}}_O \\ \dot{\boldsymbol{\omega}} \\ \ddot{\boldsymbol{q}} \end{bmatrix} + \boldsymbol{K} \begin{bmatrix} \boldsymbol{R}_O \\ \boldsymbol{\Lambda} \\ \boldsymbol{q} \end{bmatrix} = \boldsymbol{Q} \tag{26}$$

where

$$\boldsymbol{\omega} = [\omega_1 \quad \omega_2 \quad \omega_3]^T \tag{27}$$

$$\boldsymbol{M} = \begin{bmatrix} m_{\mathrm{tot}} \boldsymbol{I}_3 & -\tilde{\boldsymbol{S}}_f & \boldsymbol{C}_t \\ \tilde{\boldsymbol{S}}_f & \boldsymbol{J}_f & \boldsymbol{C}_r \\ \boldsymbol{C}_t^T & \boldsymbol{C}_r^T & \boldsymbol{M}_f \end{bmatrix} \tag{28}$$

$$\boldsymbol{K} = \begin{bmatrix} \boldsymbol{0}_{3\times 3} & \boldsymbol{0}_{3\times 4} & \boldsymbol{0}_{3\times n} \\ \boldsymbol{0}_{3\times 3} & \boldsymbol{0}_{3\times 4} & \boldsymbol{0}_{3\times n} \\ \boldsymbol{0}_{n\times 3} & \boldsymbol{0}_{n\times 4} & \boldsymbol{K}_f \end{bmatrix} \tag{29}$$

$$\boldsymbol{Q} = [\boldsymbol{Q}_t^T \quad \boldsymbol{Q}_r^T \quad \boldsymbol{Q}_f^T]^T \tag{30}$$

Neglecting the high-order terms of the deformation which are time-consuming [7], the matrices in Eqs. (28–30) are expressed as

$$\boldsymbol{S}_f = \begin{bmatrix} \int_V x \,\mathrm{d}m - \boldsymbol{q}^T \boldsymbol{C}_x \boldsymbol{q}/2 \\ \int_V y \,\mathrm{d}m - \boldsymbol{q}^T \boldsymbol{C}_y \boldsymbol{q}/2 \\ \int_V z \,\mathrm{d}m + \boldsymbol{G}\boldsymbol{q} \end{bmatrix} \tag{31}$$

$$\boldsymbol{C}_t = \begin{bmatrix} -\boldsymbol{q}^T \boldsymbol{C}_x \\ -\boldsymbol{q}^T \boldsymbol{C}_y \\ \boldsymbol{G} \end{bmatrix} \tag{32}$$

$$\boldsymbol{C}_r = \begin{bmatrix} \boldsymbol{U}_y \\ -\boldsymbol{U}_x \\ \boldsymbol{q}^T (\boldsymbol{D}_{yx} - \boldsymbol{D}_{xy}) \end{bmatrix} \tag{33}$$

$$\boldsymbol{J}_f = \begin{bmatrix} \int_V (y^2 + z^2) \,\mathrm{d}m & -\int_V xy \,\mathrm{d}m & -\int_V xz \,\mathrm{d}m \\ -\int_V xy \,\mathrm{d}m & \int_V (x^2 + z^2) \,\mathrm{d}m & -\int_V yz \,\mathrm{d}m \\ -\int_V xz \,\mathrm{d}m & -\int_V yz \,\mathrm{d}m & \int_V (x^2 + y^2) \,\mathrm{d}m \end{bmatrix} + \begin{bmatrix} \boldsymbol{q}^T (\boldsymbol{M}_f - \boldsymbol{D}_{yy}) \boldsymbol{q} & \boldsymbol{q}^T (\boldsymbol{D}_{xy} + \boldsymbol{D}_{yx}) \boldsymbol{q}/2 & -\boldsymbol{U}_x \boldsymbol{q} \\ \boldsymbol{q}^T (\boldsymbol{D}_{xy} + \boldsymbol{D}_{yx}) \boldsymbol{q}/2 & \boldsymbol{q}^T (\boldsymbol{M}_f - \boldsymbol{D}_{xx}) \boldsymbol{q} & -\boldsymbol{U}_y \boldsymbol{q} \\ -\boldsymbol{U}_x \boldsymbol{q} & -\boldsymbol{U}_y \boldsymbol{q} & -\boldsymbol{q}^T (\boldsymbol{D}_{xx} + \boldsymbol{D}_{yy}) \boldsymbol{q} \end{bmatrix} \tag{34}$$

$$\boldsymbol{Q}_t = \boldsymbol{F}_t + \begin{bmatrix} \dot{\boldsymbol{q}}^T \boldsymbol{C}_x \dot{\boldsymbol{q}} \\ \dot{\boldsymbol{q}}^T \boldsymbol{C}_y \dot{\boldsymbol{q}} \\ 0 \end{bmatrix} - \tilde{\boldsymbol{\omega}}\, \tilde{\boldsymbol{\omega}}\, \boldsymbol{S}_f - 2\tilde{\boldsymbol{\omega}} \boldsymbol{C}_t \dot{\boldsymbol{q}} \tag{35}$$

$$\boldsymbol{Q}_r = \boldsymbol{F}_r - \begin{bmatrix} 0 \\ 0 \\ \dot{\boldsymbol{q}}^T (\boldsymbol{D}_{yx} - \boldsymbol{D}_{xy}) \dot{\boldsymbol{q}} \end{bmatrix} - \tilde{\boldsymbol{\omega}} \boldsymbol{J}_f \boldsymbol{\omega} - 2 \begin{bmatrix} \boldsymbol{q}^T (\boldsymbol{M}_f - \boldsymbol{D}_{yy}) \dot{\boldsymbol{q}} & \boldsymbol{q}^T \boldsymbol{D}_{yx} \dot{\boldsymbol{q}} & 0 \\ \boldsymbol{q}^T \boldsymbol{D}_{xy} \dot{\boldsymbol{q}} & \boldsymbol{q}^T (\boldsymbol{M}_f - \boldsymbol{D}_{xx}) \dot{\boldsymbol{q}} & 0 \\ -\boldsymbol{U}_x \dot{\boldsymbol{q}} & -\boldsymbol{U}_y \dot{\boldsymbol{q}} & -\boldsymbol{q}^T (\boldsymbol{D}_{xx} + \boldsymbol{D}_{yy}) \dot{\boldsymbol{q}} \end{bmatrix} \boldsymbol{\omega} \tag{36}$$

$$\boldsymbol{Q}_f = \boldsymbol{F}_f + \omega_1^2 (\boldsymbol{M}_f - \boldsymbol{D}_{yy}) \boldsymbol{q} + \omega_2^2 (\boldsymbol{M}_f - \boldsymbol{D}_{xx}) \boldsymbol{q} + \omega_1 \omega_2 (\boldsymbol{D}_{xy} + \boldsymbol{D}_{yx}) \boldsymbol{q} - \omega_3^2 (\boldsymbol{D}_{xx} + \boldsymbol{D}_{yy}) \boldsymbol{q} - \omega_3 (\omega_2 \boldsymbol{U}_y + \omega_1 \boldsymbol{U}_x)^T \tag{37}$$

and

$$\boldsymbol{C}_x = \int_V \boldsymbol{H}_x \,\mathrm{d}m \tag{38}$$

$$\boldsymbol{C}_y = \int_V \boldsymbol{H}_y \,\mathrm{d}m \tag{39}$$

$$\boldsymbol{G} = \int_V \boldsymbol{\Phi} \,\mathrm{d}m \tag{40}$$

$$\boldsymbol{U}_x = \int_V x\boldsymbol{\Phi} \,\mathrm{d}m \tag{41}$$

$$\boldsymbol{U}_y = \int_V y\boldsymbol{\Phi} \,\mathrm{d}m \tag{42}$$

$$\boldsymbol{D}_{xx} = \int_V x\boldsymbol{H}_x \,\mathrm{d}m \tag{43}$$

$$\boldsymbol{D}_{yy} = \int_V y\boldsymbol{H}_y \,\mathrm{d}m \tag{44}$$

$$\boldsymbol{D}_{xy} = \int_V x\boldsymbol{H}_y \,\mathrm{d}m \tag{45}$$

$$\boldsymbol{D}_{yx} = \int_V y\boldsymbol{H}_x \,\mathrm{d}m \tag{46}$$

are the modal integral constants that can be calculated cumulatively using the lumped mass approach. Moreover, while normalizing the mode shapes by modal mass, as

$$\boldsymbol{M}_f = \int_V \boldsymbol{\Phi}^T \boldsymbol{\Phi}\, \mathrm{d}m = \boldsymbol{I}_n \tag{47}$$

the modal stiffness matrix can be written as

$$\boldsymbol{K}_f = \mathrm{diag}(\Omega_1^2, \Omega_2^2, \ldots, \Omega_n^2) \tag{48}$$

Noting that

$$\dot{\boldsymbol{\Lambda}} = \tfrac{1}{2}\boldsymbol{L}^T\boldsymbol{\omega} \tag{49}$$

where

$$\boldsymbol{L} = \begin{bmatrix} -\lambda_1 & \lambda_0 & \lambda_3 & -\lambda_2 \\ -\lambda_2 & -\lambda_3 & \lambda_0 & \lambda_1 \\ -\lambda_3 & \lambda_2 & -\lambda_1 & \lambda_0 \end{bmatrix} \tag{50}$$

Equations (26) can be converted to the state-space form as

$$\begin{bmatrix} \boldsymbol{0}_{(6+n)\times(7+n)} & \boldsymbol{M} \\ \boldsymbol{I}_{(7+n)} & \boldsymbol{0}_{(7+n)\times(6+n)} \end{bmatrix} \dot{\boldsymbol{d}} + \begin{bmatrix} \boldsymbol{K} & \boldsymbol{0}_{(6+n)} \\ \boldsymbol{0}_{(7+n)} & \boldsymbol{T} \end{bmatrix} \boldsymbol{d} = \begin{bmatrix} \boldsymbol{Q} \\ \boldsymbol{0}_{(7+n)} \end{bmatrix} \tag{51}$$

where

$$\boldsymbol{d} = [\, \boldsymbol{R}_O^T \quad \boldsymbol{\Lambda}^T \quad \boldsymbol{q}^T \quad \dot{\boldsymbol{R}}_O^T \quad \boldsymbol{\omega}^T \quad \dot{\boldsymbol{q}}^T \,]^T \tag{52}$$

$$\boldsymbol{T} = \begin{bmatrix} -\boldsymbol{I}_3 & \boldsymbol{0}_{3\times 3} & \boldsymbol{0}_{3\times n} \\ \boldsymbol{0}_{4\times 3} & -\boldsymbol{L}^T/2 & \boldsymbol{0}_{4\times n} \\ \boldsymbol{0}_{n\times 3} & \boldsymbol{0}_{n\times 3} & -\boldsymbol{I}_n \end{bmatrix} \tag{53}$$

For given initial states and externally applied forces, the system responses can be calculated by MATLAB function `ode45` for performing fourth- or fifth-order Runge–Kutta integration.

III. Finite Element Modeling

A high-fidelity finite element model of the solar sail is needed for modal analysis and providing verification with the reduced model. This work is conducted in ABAQUS v6.8-1. The five-point connected square sail reported in [4] is adapted here for instance, as shown in Fig. 2. Details of the finite element model are described in the following, and the material properties are summarized in Table 1 [4].

The model has four booms. The booms are 106 m thin-walled pipes, each with a pipe cross section of radius 0.229 m and thickness 7.5 μm. Each boom is meshed with 24 B31 beam elements.

The model has four sail membranes. The sail membranes are triangular films of thickness 2.50 μm with metallic coatings. Each sail membrane is meshed with 864 S3 shell elements, connecting to the booms at the three corners through cables.

The model has 12 cables. There are four 0.42 m long cables at the hub of the solar sail and eight 0.67 m long cables at the free ends of the booms. Each cable has a solid circular cross section of radius 0.5 mm. Each cable is modeled as a single T3D2 truss element.

The model has a control mast. The control mast is a 2 m thin-walled pipe, directed along the z axis from the hub. It has a pipe cross section of radius 0.01705 m and thickness 0.005 m. As the mast has a much higher fundamental frequency than the boom-sail system [4], it is modeled as a single B31 beam element.

The model has several concentrated masses. A concentrated mass representing a 0.58 kg tip plate is located at the free end of each boom, which is used for attitude control. A concentrated mass representing a 228 kg payload mass is located at the free end of the control mast. A concentrated mass representing a 54.84 kg stowage is located at the hub.

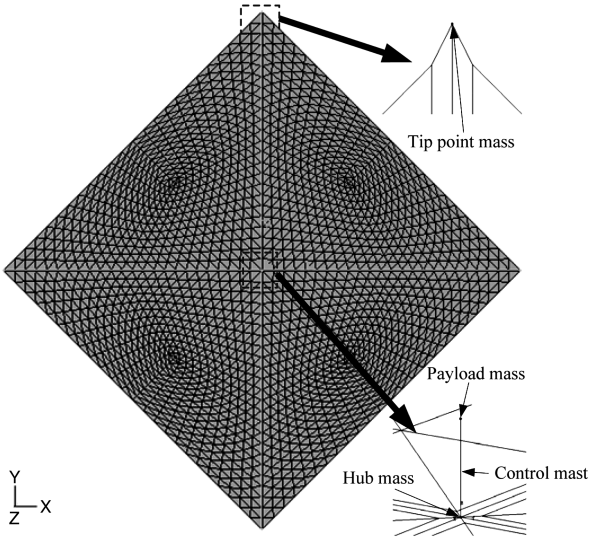

Fig. 2 Finite element model of the solar sail.

A. Pretensioning and Modal Analysis in ABAQUS/Standard

As mentioned in [4], the sail membranes were pretensioned by inducing contraction of the cables. The pretension loads were induced by a fictitious temperature reduction of the cables, which were assigned a nonzero coefficient of thermal expansion. However, this kind of pretensioning scheme is not well supported by the import analysis, while transferring results from ABAQUS/Standard to ABAQUS/Explicit for transient dynamic simulations. Consequently, a different pretensioning scheme is used here as defining initial conditions of stress on the cables. The initial stress of 0.19 GPa is assigned on the four cables at the hub of the solar sail, and the initial stress of 0.12 GPa is assigned on the eight cables at the free ends of the booms. The hub node is fixed in order to define a fixed–free boundary condition for static analysis. A geometrically nonlinear static analysis step is run, and the obtained minimum von Mises stress is 6854 Pa on the sail membrane regions.

In the next step, another geometrically nonlinear static analysis is performed to apply a solar pressure load of 9.12×10^{-6} Pa. The pressure load is defined on the four sail membranes as a surface traction in the positive z direction. In the final frame of this step, the obtained minimum von Mises stress is 10,030 Pa and the maximum deflection is 0.8658 m on the sail membrane regions.

Following the two static analysis steps of pretensioning, a modal analysis step is run to generate frequencies and mode shapes of the solar sail using the default Lanczos eigensolver. The first three non-rigid-body mode shapes are shown in Fig. 3. Element matrices are listed in a file for integrating the global lumped mass matrix. Noting that the concentrated masses are not listed in the element matrix file, they should be added in the programming effort. Node coordinates and displacements are listed in individual files for calculating the modal integral constants. Thanks to the S3 shell elements that model the sail membranes, the rotational displacements of each mode shape

Table 1 Material properties of the solar sail

Components	Density, kg/m^3	Young's modulus, Pa	Poisson's ratio
Booms	1908	124×10^9	0.30
Membrane	1572	2.48×10^9	0.34
Cables	1440	62×10^9	0.36
Control mast	7660	124×10^9	0.30

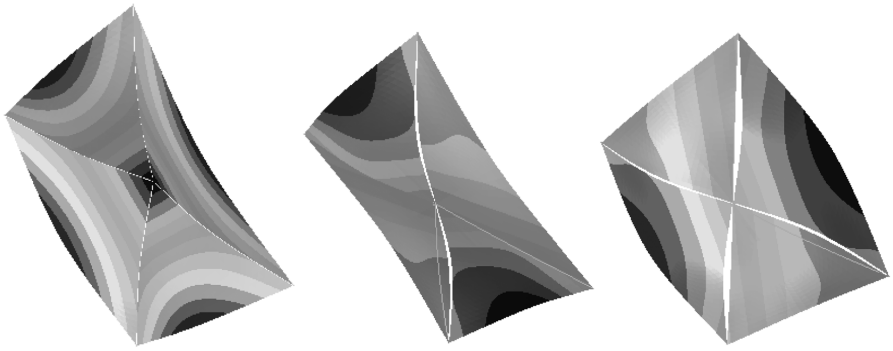

a) b) c)

Fig. 3 First three non-rigid-body mode shapes of the solar sail: a) mode 1 (0.009245 Hz), b) mode 2 (0.012877 Hz), and c) mode 3 (0.012877 Hz).

can be obtained. Thus, the modal integral constants associated with the slopes of mode shapes become easier to calculate.

B. Import Analysis and Transient Dynamic Simulations in ABAQUS/Explicit

To compute the dynamic responses of the solar sail during maneuvers, the pretensioned model in ABAQUS/Standard is transferred into ABAQUS/Explicit for transient dynamic simulations. The transfer is performed by an import analysis that creates a part from the output database by ABAQUS/Standard. The deformed configuration in the last frame of the first static analysis step is imported. The corresponding state field is defined as the initial state field. Boundary conditions, external loads, and concentrated masses cannot be imported. Thus, the tip point masses, the hub mass, and the payload mass must be defined again in the import analysis. Afterward, an explicit dynamic analysis step is performed, in which external loads due to the solar pressure and the history output requests are defined. Two Pentium 2.50 GHz processors with 1.99 GB of RAM are used for parallel computing. Inertial properties of the whole model are calculated automatically by ABAQUS/Explicit and are shown in Table 2. The simulation results are shown and examined in the next section.

IV. Comparative Studies

The reduced model retaining the first three non-rigid-body modes is compared with the finite element model in ABAQUS/Explicit through transient dynamic simulations. All damping effects are out of consideration for maximizing the vibration responses. The foreshortening effects of the solar sail during different maneuvers are studied.

A. Example of Translational Maneuver

It is assumed that the free solar sail, initially at rest, suffers from a solar pressure load of 9.12×10^{-6} Pa along the z axis. Consequently, the whole solar sail is accelerated in the positive Z direction with rigid-flexible coupling. The simulation results using different models are compared in Fig. 4.

Figures 4a and 4b represent the displacement and the velocity at the hub. As can be seen, the rigid-body motion is obviously influenced by the flexible vibration. Figures 4c and 4d represent the stretching and the deflection at tip 1. In spite that the reduced model obtains a little larger amplitudes of vibration, the foreshortening formulation is well verified by ABAQUS/Explicit. Moreover, the conventional formulation agrees well with the foreshortening formulation except for the tip stretching response. However, the tip stretching response is quite small, which means the foreshortening effects are insignificant for this instance.

B. Example of Rotational Maneuver

Based on the last example, a concentrated force of 0.01 N aroused by the solar pressure load on the tip plate is added on tip 3, initially along the z axis. The additional force follows nodal rotation, making a rotational maneuver. The solar pressure load is idealized as constant here, which is reasonable for small angle rotation. Again, the simulation results using the different models are compared in Fig. 5.

Figures 5a and 5b represent the angular displacement and the angular velocity at the hub. The angular velocity at the hub obtained by ABAQUS/Explicit is oscillating at high frequencies probably due to high-order modes or numerical errors. Figures 5c and 5d represent the stretching and the deflection at tip 1. The comparisons are similar to those in the translational case. In spite of slightly larger response errors, the reduced model can be also verified for this rotational case with the finite element model. In this example, the tip stretching response is still small, because the angular velocity of the solar sail is so small and the pretension has greatly increased the structural stiffness. If increasing the angular velocity or reducing the structural stiffness, the tip stretching response will raise. Consequently, the conventional formulation may lead to misleading predictions of the dynamic behavior of the solar sail, while the foreshortening formulation will still remain accurate due to its consideration of foreshortening effects.

The computational efficiency is summarized that the finite element model needs about 1 h of CPU time for performing each 100 s of simulation time using two CPUs, while the reduced model needs only several seconds of CPU time for a whole simulation using one CPU. Thus, the reduced model totally meets the demand of real-time control.

C. Time-Varying Properties

In practice, the solar pressure load varies with the position and the attitude of the solar sail relative to the sun. The modal characteristics of the solar sail are influenced by the solar pressure load and the inertial forces. Therefore, the reduced model using constant solar pressure loads and modal parameters is reasonable only if these properties do not vary too much during the simulation time. For simulating long-term maneuvers, a time-varying solar pressure load should be modeled. Correspondingly, the modal parameters of the solar sail should be revised with time to reduce cumulative errors.

Table 2 Inertial properties of the solar sail

Total mass, kg	Center of mass in $Oxyz$, m	Moments of inertia about O, kg · m^2					
		I_{xy}	I_{yy}	I_{zz}	I_{xy}	I_{yz}	I_{zx}
387.72	(0, 0, 1.19416)	1.92267×10^5	1.92267×10^5	3.82635×10^5	0	0	0

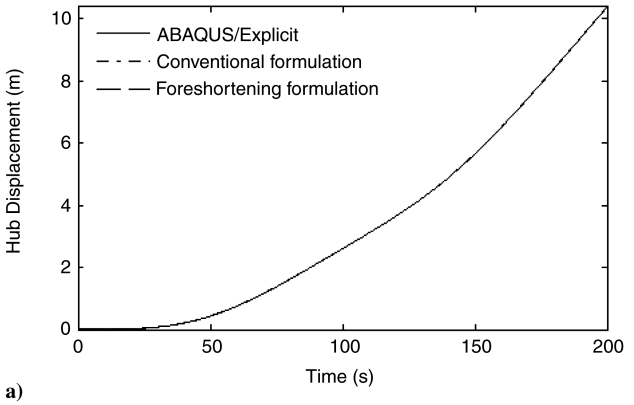

a)

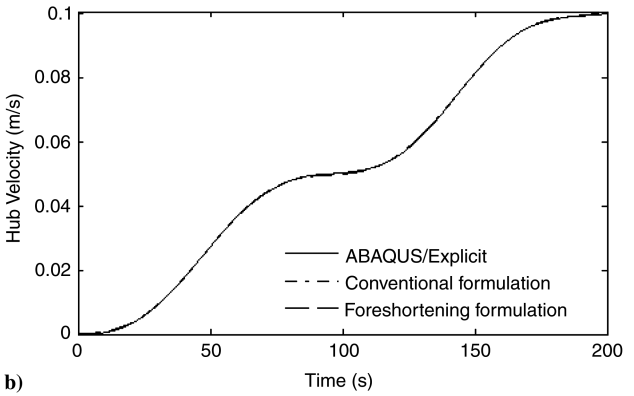

b)

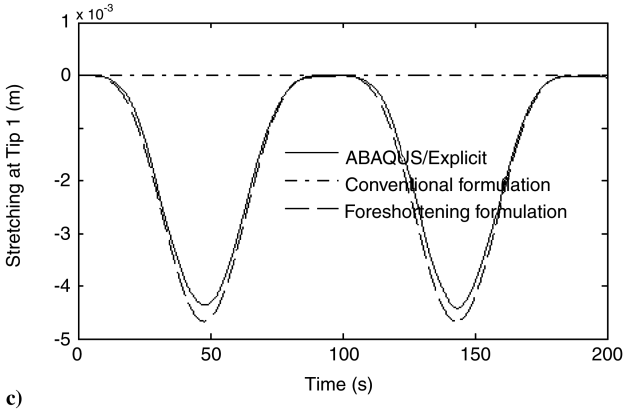

c)

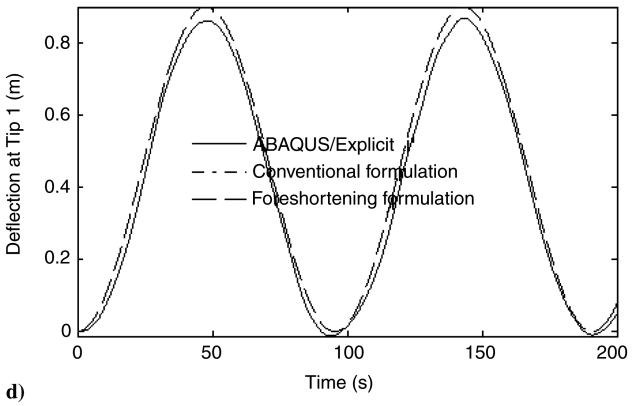

d)

Fig. 4 Dynamic responses during the translational maneuver: a) hub displacement, b) hub velocity, c) stretching response at tip 1, and d) deflection at tip 1.

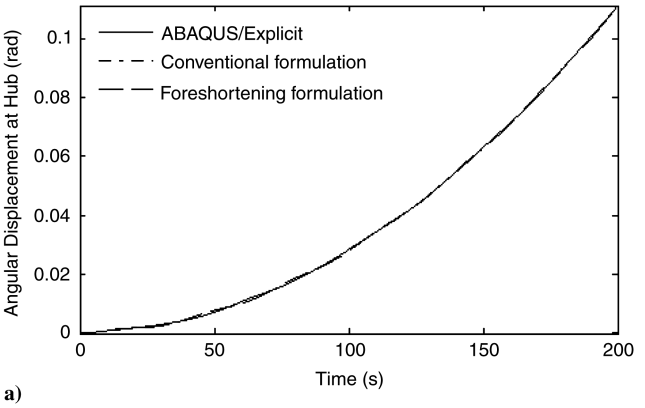

a)

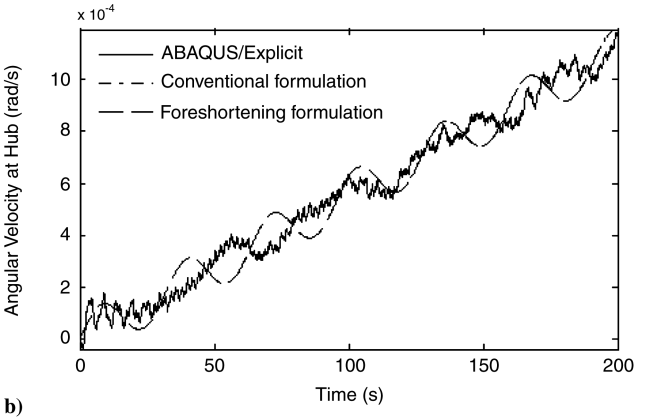

b)

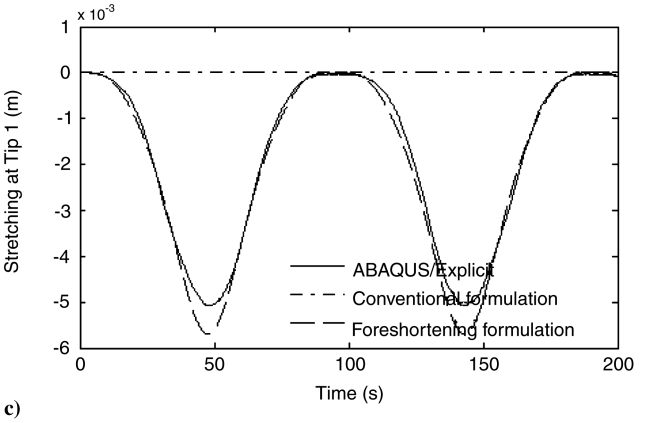

c)

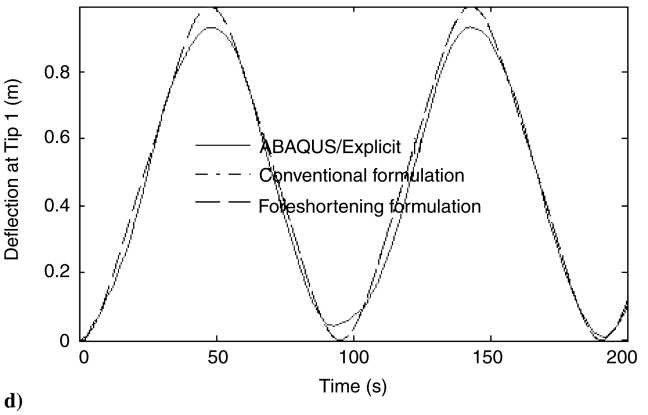

d)

Fig. 5 Dynamic responses during the rotational maneuver: a) hub angular displacement, b) hub angular velocity, c) stretching response at tip 1, and d) deflection at tip 1.

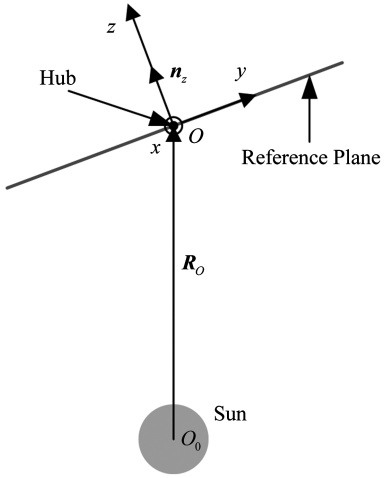

Fig. 6 Solar pressure load schematic.

As shown in Fig. 6, the solar pressure load is supposed uniform on the reference plane and parallel to $\boldsymbol{n}_z$. Thus, the solar pressure load vector is defined as

$$\boldsymbol{p}_s = \boldsymbol{n}_z \cdot \frac{p_O \boldsymbol{R}_O}{|\boldsymbol{R}_O|} \boldsymbol{n}_z \tag{54}$$

where

$$p_O = \frac{2I_s}{4\pi c |\boldsymbol{R}_O|^2} \tag{55}$$

where $I_s = 4 \times 10^{26}$ W, $c = 3 \times 10^8$ m/s.

Initially, the static solar sail is normal to the sunlight with $|\boldsymbol{R}_O| = 1.5254 \times 10^{11}$ m, where $p_O = 9.12 \times 10^{-6}$ Pa. As the resultant of solar pressure load on the tip plate at tip 3, a concentrated force of 0.01 N is applied on tip 3 along the z axis, which makes the solar sail rotate. The solar pressure loads on the reference plane and the tip plate are time-varying according to Eq. (54). As ABAQUS does not provide a convenient tool for defining a solution-dependent load, the time history of the solar pressure load obtained using the reduced model is transplanted to the finite element model in ABAQUS through tabular input.

To simulate the time-varying modal characteristics of the solar sail, several modal analyses are conducted. During the modal analyses, different solar pressure loads and the deduced rigid-body accelerations are considered. Inertial forces are modeled as gravities with the accelerations in the negative direction, identified as pseudo inertia relief [3]. Using the pseudo inertia relief, the modal frequencies versus different solar pressure loads are listed in Table 3. In the revision of our reduced model, the modal stiffness matrix is varying with the solar pressure load by a Lagrange interpolation formula according to the data in Table 3. As the mode shapes are quite similar under the different loads, the modal integral constants in the revised model are calculated only once using the mode shapes shown in Fig. 3 for keeping high efficiency.

As shown in Fig. 7, the original model refers to the foreshortening formulation model using the constant modal stiffness matrix; the revised model refers to the foreshortening formulation model using

Table 3 Modal frequencies versus different solar pressure loads under pseudo inertia relief

Solar pressure load, $\times 9.12$ μPa	Mode 1, $\times 10^{-3}$ Hz	Mode 2 and 3, $\times 10^{-2}$ Hz
0	8.97923	1.05492
0.2	9.03306	1.06165
0.4	9.12915	1.07474
0.6	9.20158	1.08972
0.8	9.23770	1.10390
1	9.24898	1.11625

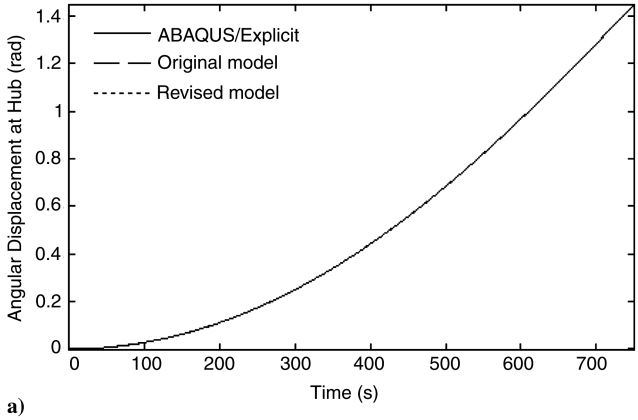

a)

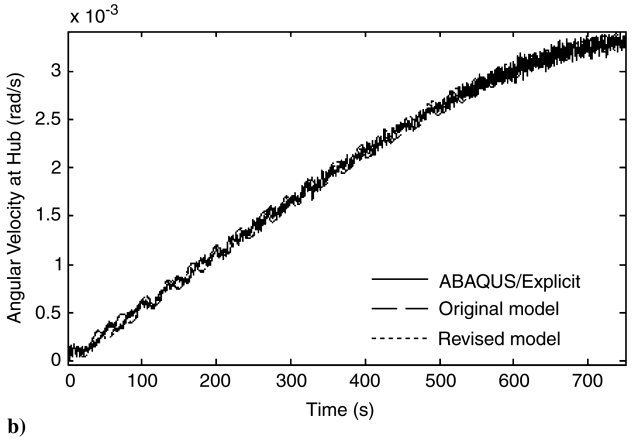

b)

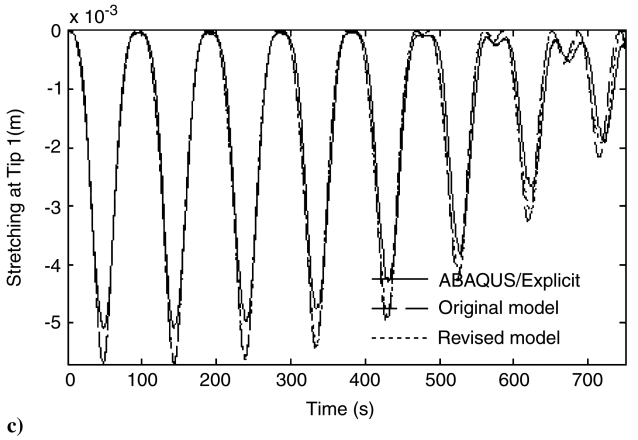

c)

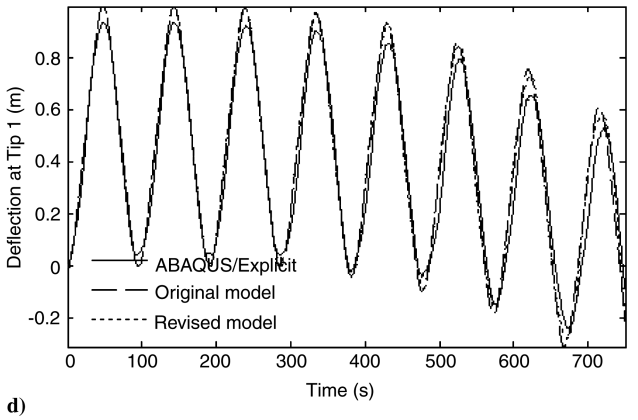

d)

Fig. 7 Dynamic responses during the long-term rotational maneuver: a) hub angular displacement, b) hub angular velocity, c) stretching response at tip 1, and d) deflection at tip 1.

the time-varying modal stiffness matrix described in the last paragraph. The original model still shows acceptable accuracy, especially for the rigid-body motion. This is because that the modal frequencies of the solar sail vary with the solar pressure load very slightly for the case studied. However, the revised model seems more accurate than the original model for long-term simulations. For an inner solar system mission where the solar pressure is much stronger, such as a Mercury orbiter, the revised model would show more advantages.

V. Conclusions

For dynamics and control design of a flexible solar sail, a reduced model in mixed coordinates considering foreshortening effects was formulated. As a benchmark, a high-fidelity finite element model of a five-point connected square solar sail was modeled in ABAQUS. The prestressed modes of the solar sail obtained using ABAQUS/Standard were used for modal reduction in the reduced model. The finite element model with pretension was transferred from ABAQUS/Standard to ABAQUS/Explicit to verify the reduced model by dynamic responses. The dynamic responses during different maneuvers were compared. Good consistency was obtained between the reduced model and the finite element model. A time-varying modal stiffness matrix was used in the reduced model to reveal the influence of the time-varying solar pressure load during long-term maneuvers. It can be concluded that the proposed reduced model is accurate and efficient, and it appears ready for dynamics and control design of practical solar sails.

Acknowledgment

This work was supported by the National Natural Science Foundation of China (No. 10832004).

References

[1] Friedman, L., *Starsailing: Solar Sails and Interstellar Travel*, Wiley, New York, 1988.

[2] McInnes, C. R., *Solar Sailing: Technology, Dynamics and Mission Applications*, Springer, London, 1999.

[3] Taleghani, B. K., Sleight, D. W., Muheim, D. M., Belvin, K., and Wang, J. T., "Assessment of Analysis Approaches for Solar Sail Structural Response," 39th AIAA/ASME/SAE/ASEE Joint Propulsion Conference and Exhibit, Huntsville, AL, AIAA Paper 2003-4796, 2003.

[4] Sleight, D. W., and Muheim, D. M., "Parametric Studies of Square Solar Sails Using Finite Element Analysis," 45th AIAA/ASME/ASCE/AHS/ASC Structures, Structural Dynamics & Materials Conference, Palm Springs, CA, AIAA Paper 2004-1509, 2004.

[5] Smith, S. W., Song, H., Baker, J. R., Black, J., and Muheim, D. M., "Flexible Models for Solar Sail Control," 46th AIAA/ASME/ASCE/AHS/ASC Structures, Structural Dynamics & Materials Conference, Austin, TX, AIAA Paper 2005-1801, 2005.

[6] Bathe, K.-J., *Finite Element Procedures*, Prentice–Hall, Upper Saddle River, NJ, 1996.

[7] Lugrís, U., Naya, M. A., Pérez, J. A., and Cuadrado, J., "Implementation and Efficiency of Two Geometric Stiffening Approaches," *Multibody System Dynamics*, Vol. 20, No. 2, 2008, pp. 147–161. doi:10.1007/s11044-008-9114-6

[8] Mayo, J. M., García-Vallejo, D., and Domínguez, J., "Study of the Geometric Stiffening Effect: Comparison of Different Formulations," *Multibody System Dynamics*, Vol. 11, No. 4, 2004, pp. 321–341. doi:10.1023/B:MUBO.0000040799.63053.d9

[9] Shabana, A. A., *Dynamics of Multibody Systems*, Cambridge Univ. Press, New York, 2005.

C. Kluever
Associate Editor